


An inexpensive microfluidic device for three-dimensional hydrodynamic focusing in imaging flow cytometry


Cite as: Biomicrofluidics **14**, 064110 (2020); <https://doi.org/10.1063/5.0033291>

Submitted: 15 October 2020 . Accepted: 13 November 2020 . Published Online: 14 December 2020

Yogesh M. Patel, Sanidhya Jain, Abhishek Kumar Singh, Kedar Khare, Sarita Ahlawat, and  Supreet Singh Bahga

COLLECTIONS

 This paper was selected as Featured

 This paper was selected as Scilight



View Online



Export Citation



CrossMark

ARTICLES YOU MAY BE INTERESTED IN

[Inexpensive microfluidic device enables the imaging of cells one-by-one](#)
Scilight **2020**, 511101 (2020); <https://doi.org/10.1063/10.0002967>

[Microfluidic compartmentalization to identify gene biomarkers of infection](#)
Biomicrofluidics **14**, 061502 (2020); <https://doi.org/10.1063/5.0032849>

[Size and shape based chromosome separation in the inertial focusing device](#)
Biomicrofluidics **14**, 064109 (2020); <https://doi.org/10.1063/5.0026281>



Biophysics Reviews

First Articles Now Online!

READ NOW >>>



An inexpensive microfluidic device for three-dimensional hydrodynamic focusing in imaging flow cytometry



Cite as: *Biomicrofluidics* 14, 064110 (2020); doi: [10.1063/5.0033291](https://doi.org/10.1063/5.0033291)
Submitted: 15 October 2020 · Accepted: 13 November 2020 ·
Published Online: 14 December 2020



Yogesh M. Patel,¹ Sanidhya Jain,¹ Abhishek Kumar Singh,¹ Kedar Khare,² Sarita Ahlawat,³
and Supreet Singh Bahga^{1,a)}

AFFILIATIONS

¹Department of Mechanical Engineering, Indian Institute of Technology Delhi, New Delhi 110016, India

²Department of Physics, Indian Institute of Technology Delhi, New Delhi 110016, India

³Phase Laboratories Pvt. Ltd., Technology Based Incubation Unit, Indian Institute of Technology Delhi, New Delhi 110016, India

^{a)}Author to whom correspondence should be addressed: bahga@mech.iitd.ac.in

ABSTRACT

We present design, characterization, and testing of an inexpensive, sheath-flow based microfluidic device for three-dimensional (3D) hydrodynamic focusing of cells in imaging flow cytometry. In contrast to other 3D sheathing devices, our device hydrodynamically focuses the cells in a single-file near the bottom wall of the microchannel that allows imaging cells with high magnification and low working distance objectives, without the need for small device dimensions. The relatively large dimensions of the microchannels enable easy fabrication using less-precise fabrication techniques, and the simplicity of the device design avoids the need for tedious alignment of various layers. We have characterized the performance of the device with 3D numerical simulations and validated these simulations with experiments of hydrodynamic focusing of a fluorescently dyed sample fluid. The simulations show that the width and the height of the 3D focused sample stream can be controlled independently by varying the heights of main and side channels of the device, and the flow rates of sample and sheath fluids. Based on simulations, we also provide useful guidelines for choosing the device dimensions and flow rates for focusing cells of a particular size. Thereafter, we demonstrate the applicability of our device for imaging a large number of RBCs using brightfield microscopy. We also discuss the choice of the region of interest and camera frame rate so as to image each cell individually in our device. The design of our microfluidic device makes it equally applicable for imaging cells of different sizes using various other imaging techniques such as phase-contrast and fluorescence microscopy.

Published under license by AIP Publishing. <https://doi.org/10.1063/5.0033291>

I. INTRODUCTION

Flow cytometry is a widely used method for counting and characterization of cells from a heterogeneous cell suspension^{1,2} and has found application in numerous fields including disease diagnosis, clinical trials, and basic research.³⁻⁷ In a typical flow cytometer, cells are focused into a single-file arrangement to ensure that they pass one-by-one through a probe volume, where they are detected by an optical point-detector.^{2,8} Although conventional flow cytometers can characterize cells at high rates of over 50 000 cells/s, the complexity of these systems makes them prone to failures, such as sample carryover, contamination, and clogging of the nozzle.^{9,10} These issues have led to the development of microfluidic

flow cytometers that offer advantages of handling small sample volumes, low-cost, and reduced contamination through the use of disposable microfluidic chips.⁹⁻¹² Moreover, the planar format of microfluidic devices allows high resolution imaging of cells, as opposed to single-point detection in conventional cytometry, thereby enabling detection based on spatially resolved information of cell morphology. This technique, wherein microfluidic flow cytometry is integrated with optical microscopy is termed imaging flow cytometry.^{13,14}

A necessary step in microfluidic imaging flow cytometry is the positioning of cells from a random suspension within the focal plane of the objective lens. This step is particularly critical for

imaging flow cytometry because microscope objectives with high magnification and numerical aperture have small depth-of-field and the cells must pass through this narrow region around the focal plane so as to be imaged sharply. In addition, the cells must flow close to the objective because the working distance of an objective decreases with the magnification. Besides positioning the cells at a particular depth in the microfluidic device, it is often convenient to simultaneously focus the cell suspension along the width so as to ensure that the cells can be imaged one-by-one as they pass through the detection volume, without the need for tracking the location of cells. Therefore, imaging flow cytometry requires that the randomly suspended cells in the inlet stream are three-dimensionally focused into a single-file arrangement, wherein one cell passes at a time through the detection volume.

Various strategies have been proposed to passively focus cells in three-dimensions without the need for an external actuation. These techniques include three-dimensional (3D) hydrodynamic focusing using sheath flows,^{15–19} the Dean flow,^{20–23} and inertial forces.^{24,25} The physical mechanisms underlying 3D cell focusing based on the Dean flow and inertial forces necessitate relatively high flow velocities of the order of 1 m/s, which limit the application of these techniques to systems with high-speed imaging of order of 10000 frames per second. On the other hand, 3D cell focusing based on sheath flows offer flexibility to operate at both low and high flow rates as the mechanism of focusing is rather independent of the flow rate.

In 3D hydrodynamic focusing based on sheath flows, the cell suspension is squeezed in three-dimensions using sheath streams of a buffer solution to such an extent that only a single cell can pass through the detection volume at a given time. This can be achieved by focusing a central stream of cells along the width using two sheath streams, followed by focusing in the depth direction by another pair of sheath streams.¹⁸ Alternatively, 3D focusing of cells can be achieved in a single step using multilayered microfluidic devices, wherein the sheath fluid flows from horizontal and vertical directions.^{16,17} Such devices enable positioning of cells at the mid-plane along the depth direction while simultaneously focusing the cell suspension along the width of the microchannel. Both of these approaches for 3D hydrodynamic focusing using sheath flows require microfluidic devices with multi-layer construction, which makes the fabrication process tedious and also increases the cost of the device. Moreover, since these techniques focus the cells at the midplane of the microchannel, it is necessary to fabricate devices with smaller depth using more precise fabrication methods to ensure that the cells flow within the working distance of the microscope objective. Since microfluidic devices for imaging flow cytometry must be disposed off after one-time use to avoid contamination, it is imperative to reduce the cost of these devices using simplified designs and low-cost fabrication techniques, without affecting the functionality.

In this paper, we present design, characterization, and testing of a microfluidic device for 3D hydrodynamic focusing of cells using sheath flows that overcomes the aforementioned challenges of other 3D sheathing devices. Our device is particularly suited for imaging flow cytometry as it focuses the cells near the bottom wall of the microfluidic chip. Consequently, even with thicker channels fabricated with less-precise fabrication methods, our device enables

accurate positioning of cells within the working distance of the objective of an inverted microscope. That is, our device design enables similar performance as other 3D sheathing devices while having larger dimensions, easier fabrication, and correspondingly lower cost. We note that the only other device reported in the literature that offers similar functionality is that by Lin *et al.*,¹⁹ wherein the sheath-flow stream is introduced perpendicular to the sample inlet to encircle and focus the cells. However, unlike their device, our device offers an additional advantage of independent control over the width and the depth of the focused cell stream, thereby allowing easy selection of device dimensions and operating parameters for 3D focusing cells and particles of different sizes.

We begin by describing the design of our 3D focusing microfluidic device and its working principle. Thereafter, through computational fluid dynamics simulations, we evaluate the performance of the device on parameters such as device dimensions and flow rates of the sample and sheath fluids. Thereafter, we confirm these simulations using experimental visualization of 3D focusing of a fluorescently dyed sample stream. Based on these simulations and experiments, we provide useful guidelines for choosing device dimensions and flow rates for specific applications. Next, we demonstrate the applicability of our device to imaging flow cytometry by imaging a large number of red blood cells. Finally, we discuss the choice of the region of interest and camera frame rate so as to image each cell individually in our device.

II. MICROFLUIDIC DEVICE DESIGN AND FABRICATION

The design of our 3D focusing microfluidic device is illustrated in Fig. 1. The device has a cross-channel geometry with the main channel and the side channels having different heights.

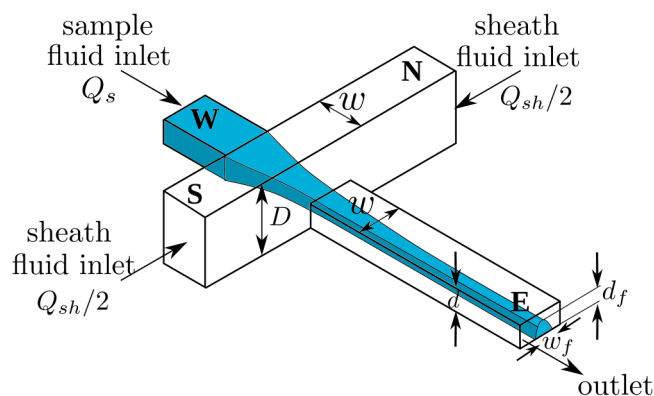


FIG. 1. Schematic of the microfluidic device for 3D hydrodynamic focusing for imaging flow cytometry. The sample enters through the W end with a flow rate of Q_s and the sheath fluid, with a total flow rate of Q_{sh} , enters symmetrically through the N and S ends of the microfluidic device. Because the height of the side channels (D) is greater than the height (d) of the channel connecting W and E ends, at the cross-junction, the sheath fluid not only focuses the sample stream along the width but also focuses it close to the bottom wall of the main channel. The width (w_f) and the height (d_f) of the focused stream can be controlled by varying the height ratio D/d and the ratio of sample and sheath-flow rates Q_s/Q_{sh} .

main channel connecting the west (W) and the east (E) reservoirs has a height d and width w , whereas the side channels that bring in the sheath fluid from north (N) and south (S) reservoirs have larger height D and the same width w . The bottom surfaces of both channels are at the same plane, and the cells are imaged from below. The cell suspension is fed into the device from the W inlet and sheath streams of the buffer solution flow in from the N and S inlets. At the junction, the sheath streams hydrodynamically focus the sample stream along the width of the channel connecting the junction and the E reservoir. Because the height of the side channels is higher than the main channel, the sheath flow also focuses the sample stream near the bottom wall of the main channel, resulting in 3D hydrodynamic focusing of the sample stream.

In the current work, the widths of all the channels w were kept fixed at $200\ \mu\text{m}$. The height of the main channel d was chosen as $100\ \mu\text{m}$. The height of the side channels D was varied from $100\ \mu\text{m}$ to $400\ \mu\text{m}$ to understand the effect of the height ratio D/d on 3D hydrodynamic focusing. The channels connecting W, N, and S reservoirs to the junction were $7.5\ \text{mm}$ long, whereas the channel connecting the junction to the E reservoir was $27.5\ \text{mm}$ long. The microchannels were fabricated on a polymethyl methacrylate (PMMA) substrate of $3\ \text{mm}$ thickness using micromilling. The microchannels were machined using a computer numerical control (CNC) machine with a carbide endmill having $200\ \mu\text{m}$ diameter. Thereafter, $2\ \text{mm}$ diameter holes were drilled at the channel ends to make the reservoirs. The milled and drilled top substrate was then cleaned with de-ionized (DI) water and isopropyl alcohol (IPA), and the open side was thermally bonded with a $0.25\ \text{mm}$ thick PMMA sheet. The thermal bonding was carried out by clamping the device and the PMMA sheet and heating them at $155\ ^\circ\text{C}$ temperature for $20\ \text{min}$ in a hot air oven. Finally, the bonded microfluidic device was cleaned by flowing IPA and DI water through all the channels. Note that, the design of our device, illustrated in Fig. 1, allows machining of all the channels having different heights on a single substrate, followed by bonding of the open side with a flat cover plate. Therefore, the fabrication of our device does not require tedious alignment of multiple layers as required by many 3D sheathing devices.^{15–17} Our device can also be fabricated with various other microfabrication techniques, such as hot embossing, laser-micromachining, and injection molding without the need for aligning different layers during the fabrication and bonding process.

III. NUMERICAL SIMULATIONS

The width (w_f) and the height (d_f) of the focused sample stream, shown schematically in Fig. 1, depend on the following dimensional parameters: (i) the device dimensions d , D , and w , (ii) the flow rate of sample fluid Q_s and the total flow rate of the sheath fluid Q_{sh} , and (iii) the density ρ and dynamic viscosity μ of fluids. Assuming that the sample and sheath fluids have similar physical properties, the dimensionless width w_f/w and height d_f/d of the focused stream depend only on the following dimensionless parameters: D/d , w/d , Q_s/Q_{sh} , and $Re = \rho Q_{sh}/(\mu w)$. Because the Reynolds number is typically small for flows in microfluidic devices, it does not affect the width and the height of the focused sample stream. Therefore, the performance of our device for 3D

hydrodynamic focusing the sample stream is governed only by the height ratio of channels (D/d), the aspect ratio of the main channel (w/d), and the ratio of flow rates of sample and sheath fluids (Q_s/Q_{sh}).

We performed 3D computational fluid dynamics (CFD) simulations to evaluate the performance of the device for 3D hydrodynamic focusing of the sample stream. In particular, we considered the effect of the varying height ratio (D/d) and the flow rate ratio (Q_s/Q_{sh}) on the width and the height of the focused stream. These simulations were performed by solving the continuity and the Navier–Stokes equations for the incompressible flow using a commercial CFD software, COMSOL Multiphysics (COMSOL, Stockholm, Sweden). The geometry of the computational domain was the same as that of the actual device. At the inlets, uniform flow velocities were prescribed as the boundary conditions, whereas at the outlet, a constant pressure boundary condition was applied. The no-slip boundary condition was applied at the walls of all microchannels. The sample and the sheath fluids were both taken as water with a density of $997.1\ \text{kg m}^{-3}$ and a dynamic viscosity of $8.91 \times 10^{-4}\ \text{Pa s}$. Appropriate grid independence tests were done to ensure the accuracy of simulations.

To calculate the width and the height of the hydrodynamically focused stream, streamlines originating from the W end of the device, corresponding to the sample inlet, were computed. These streamlines were distributed uniformly at the inlet cross section of the channel and the extreme streamlines at the outlet (E) of the device were used to obtain the width (w_f) and the height (d_f) of the focused sample stream. Figure 2 shows the cross section of the sample stream at the outlet of the main channel obtained from simulations at varying values of the height ratio D/d and the flow rate ratio Q_s/Q_{sh} , while keeping the aspect ratio fixed at $w/d = 2$.

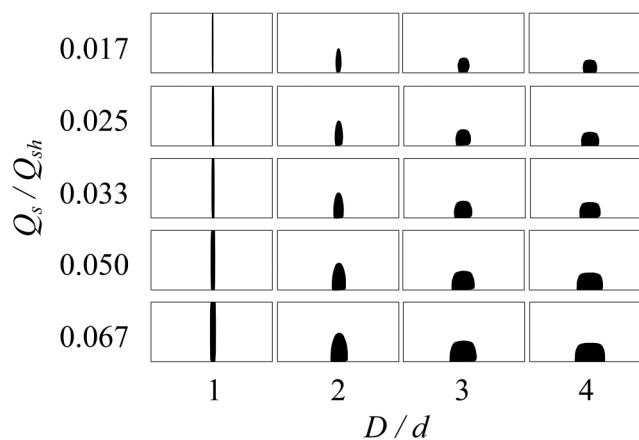


FIG. 2. Simulated cross-section of the hydrodynamically focused sample stream at the outlet (E end) of the microfluidic device for various combinations of the height ratio (D/d) and the flow rate ratio (Q_s/Q_{sh}). For $D/d = 1$, the sample stream is focused in 2D, whereas for $D/d > 1$, 3D hydrodynamic focusing is achieved. The sample stream focuses near the bottom wall of the microchannel because a fraction of sheath stream flows vertically downward at the junction and displaces the sample stream downward.

When the heights of the main channel (d) and the side channels (D) are equal, that is, $D/d = 1$, two-dimensional (2D) focusing of the sample stream occurs. Consequently, as shown in Fig. 2, the sample stream is focused throughout the depth of the main channel for $D/d = 1$. As expected, the width of the 2D focused stream decreases upon increasing the sheath flow rate or decreasing Q_s/Q_{sh} . For $D/d > 1$, the sample stream focuses three-dimensionally near the bottom surface of the main channel. For a fixed value of Q_s/Q_{sh} , the height (d_f) of the focused stream decreases upon increasing the height ratio D/d , as larger fraction of the sheath fluid flows vertically downward at the junction. Moreover, the width (w_f) of the focused stream increases upon increasing D/d for a fixed flow rate ratio, as lesser fraction of the sheath flow is available to focus the sample stream along the width. Overall, Fig. 2 shows that the desired width and the height of the focused sample stream can be obtained by controlling the height ratio D/d and the flow rate ratio Q_s/Q_{sh} .

The simulation predictions of the width and the height of the focused stream for varying values of the flow rate ratio Q_s/Q_{sh} and the height ratio D/d are presented in Figs. 3(a) and 3(b), respectively. The width of the focused sample stream increases almost linearly with the flow rate ratio Q_s/Q_{sh} . Moreover, as suggested earlier by Fig. 2, the width (w_f) of the focused stream increases with the height ratio D/d . This is because, if the height of the side channels (D) is increased while keeping all other parameters fixed, then a larger fraction of the sheath stream flows vertically near the junction to reduce the height (d_f) of the focused stream, as shown in Fig. 3(b). This reduction in the height of the focused stream is accompanied by a corresponding increase of its width to ensure mass continuity. Figure 3(b) shows an interesting characteristic of our device that the height of the focused stream d_f is primarily dependent on the height ratio D/d and weakly dependent on the flow rate ratio Q_s/Q_{sh} .

Next, we develop some simple mathematical relations to select the height ratio D/d and the flow rate ratio Q_s/Q_{sh} for obtaining desired dimensions of the focused sample stream. To this end, we note that the simulation results presented in Fig. 3(b) suggest that the height of the focused sample stream (d_f) can be approximated by

$$\frac{d_f}{d} \approx \frac{d}{D}. \tag{1}$$

Because, in practice, $Q_{sh} \gg Q_s$, the mean flow velocity downstream of the cross-junction can be approximated as $Q_{sh}/(wd)$. Therefore, on applying the continuity equation for the sample stream, upstream, and far downstream of the cross-junction, we obtain

$$Q_s \approx \frac{Q_{sh}}{wd} w_f d_f. \tag{2}$$

Finally, substituting the expression for d_f given by Eq. (1) in the above equation, we arrive at an approximate relation for the width of the focused sample stream,

$$\frac{w_f}{w} \approx \frac{Q_s D}{Q_{sh} d}. \tag{3}$$

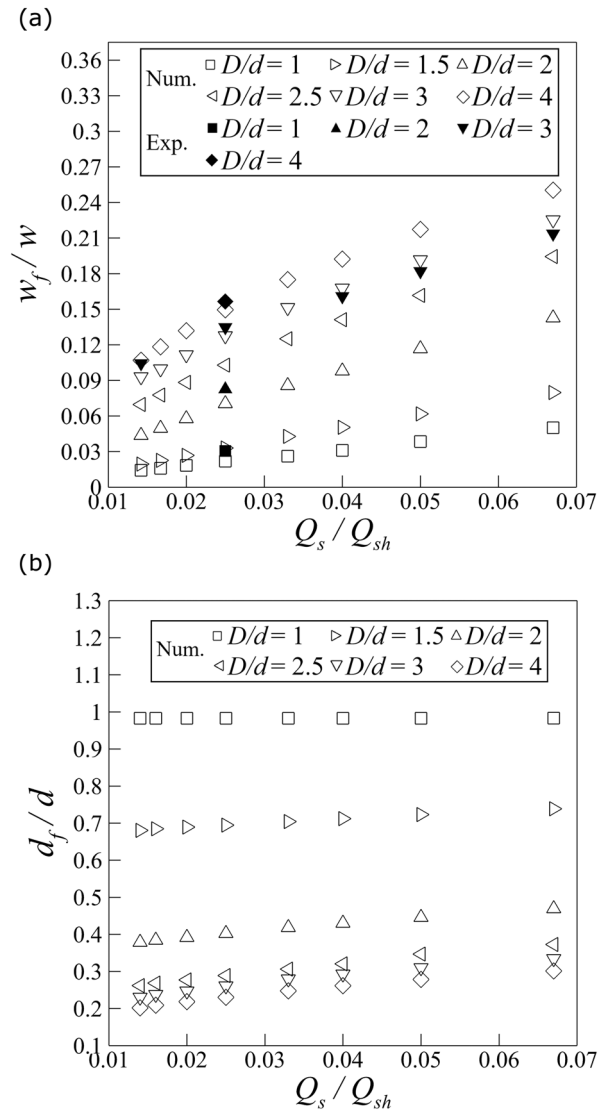


FIG. 3. Simulation predictions of the width (w_f) and height (d_f) of the focused sample stream for various combinations of the flow rate ratio (Q_s/Q_{sh}) and the height ratio (D/d), along with experimentally measured w_f . (a) The dimensionless width of the focused stream (w_f/w) increases almost linearly with Q_s/Q_{sh} . For a fixed value of Q_s/Q_{sh} , the width of the focused sample stream increases with an increase in D/d . The simulation predictions of w_f are in quantitative agreement with experimental measurements. (b) Simulated predictions of the dimensionless height of the focused sample stream (d_f/d) show that d_f depends primarily on D/d and is weakly dependent on Q_s/Q_{sh} . In particular, the height of the focused stream d_f is governed by an approximate relation $d_f/d \approx d/D$.

This relation is consistent with the simulation results presented in Fig. 3(a) that the dimensionless width (w_f/w) of the focused stream increases with an increase in Q_s/Q_{sh} and D/d . Despite their simplicity, Eqs. (1) and (3) predict approximately similar

hydrodynamic focusing characteristics as those by 3D simulations. For example, for $D/d = 4$ and $Q_s/Q_{sh} = 0.05$, the simulations shown in Fig. 3 predict $w_f/w = 0.22$ and $d_f/d = 0.28$, whereas Eqs. (1) and (3) predict $w_f/w = 0.20$ and $d_f/d = 0.25$.

Equations (1) and (3) can serve as useful rules of thumb while choosing device dimensions and flow rates to ensure that the dimensions of the focused sample stream are so small that the cells get aligned in a single file as they flow through the main channel. Moreover, these relations show that the height and the width of the focused stream can be varied independently while choosing the height ratio D/d and the flow rate ratio Q_s/Q_{sh} . For example, to achieve a desired value of d_f/d , as suggested by Eq. (1), the depth ratio D/d can be fixed first. Thereafter, the flow rate ratio (Q_s/Q_{sh}) can be chosen to obtain the desired w_f/w without affecting the height of the focused stream.

IV. EXPERIMENTS

A. Materials and methods

We performed two sets of experiments to characterize 3D hydrodynamic focusing in our microfluidic device. In the first set of experiments, the sample stream consisted of $1\ \mu\text{m}$ diameter red-fluorescent polystyrene particles (Sigma-Aldrich) suspended in DI water and Triton X-100 (Sigma-Aldrich) mixture, while the sheath fluid was DI water. The red-fluorescent particles were not used for visualizing individual particles but as tracers having low diffusivity. These set of experiments were used to validate the numerical predictions of the width (w_f) of the focused stream for varying values of the height ratio D/d and the flow rate ratio Q_s/Q_{sh} . Note that the low diffusivity of fluorescent particles compared with that of any fluorescent dye prevents bias in the measurement of w_f due to molecular diffusion of the fluorescent tracer. The flow rate of the sample stream Q_s was fixed at $1\ \mu\text{l}/\text{min}$, and the total flow rate of sheath stream Q_{sh} was varied to achieve different values of Q_s/Q_{sh} . The 3D focused sample stream was visualized using an inverted epifluorescence microscope (TS100-F, Nikon, Japan) equipped with a $10\times$ objective (CFI Achromat, NA = 0.25) and a CCD camera (PCO Pixelfly, PCO AG, Germany).

The second set of experiments were performed to image and count red blood cells (RBCs) using our 3D hydrodynamic focusing microdevice. Hydrodynamic focusing of RBCs serves as a challenging test case to demonstrate the device operation as their small size requires smaller width and height of the focused sample stream to align them in a single file arrangement. In these experiments, the sample fluid consisted of RBCs mixed in $1\times$ phosphate buffered saline (PBS) solution and the sheath fluid was $1\times$ PBS buffer. The hydrodynamically focused RBCs were visualized using the microscopy setup described above, but in the brightfield mode using $10\times$ and $40\times$ (CFI Achromat LWD, NA = 0.55) objectives. Another set of experiments were performed for brightfield imaging of a large number of RBCs at a higher imaging rate, for which we used an inverted microscope (HO-DHM-UT01, Holmarc, India) equipped with $20\times$ objective (Plan Fluor, ELWD, NA = 0.45) and a CMOS camera (IDS, Germany). The acquired images were processed by subtracting the background image acquired prior to flowing the RBCs.

In all the experiments, the sample fluid was introduced from the W reservoir using a single-channel syringe pump (Legato 110, KD Scientific, USA), whereas the sheath fluid was introduced from N and S reservoirs using a dual-channel syringe pump (Legato 210, KD Scientific, USA). The syringes of sample and sheath fluids were connected to the reservoirs via pressure monitoring tubes. Prior to start of every experiment, all the microchannels are primed with the sheath fluid.

B. Visualization of 3D hydrodynamic focusing

Figure 4(a) shows a typical time-averaged snapshot of 3D hydrodynamic focusing of the fluorescently dyed sample stream at $Q_s/Q_{sh} = 0.025$ in a microfluidic device with $D/d = 4$. The fluorescently dyed stream attains an asymptotic width at a small distance downstream of the cross junction. The reduced fluorescence intensity of the focused stream in Fig. 4(a) compared with the inlet stream suggests that the sample stream was focused three-dimensionally close to the bottom wall of the main channel; this was also verified by imaging at different planes along the depth of the microchannel. Using time-averaged snapshots, such as that shown in Fig. 4(a), we calculated the width of the focused stream

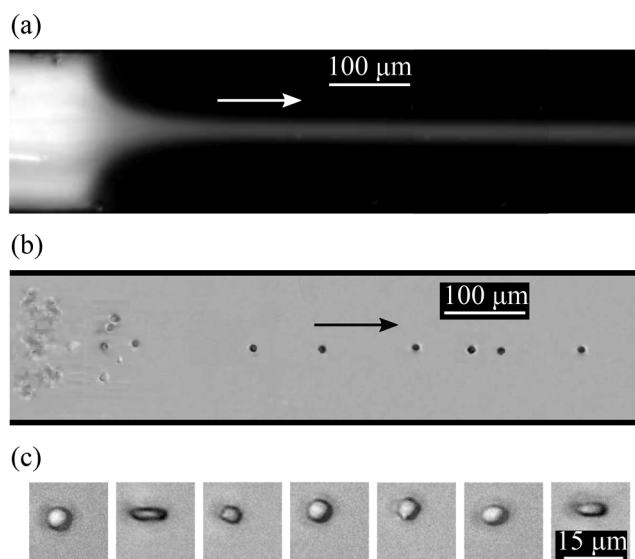


FIG. 4. Experimental visualization of 3D hydrodynamic focusing using a fluorescently dyed sample stream and RBCs. (a) Time-averaged snapshot of 3D hydrodynamic focusing of fluorescently dyed sample stream for $Q_s/Q_{sh} = 0.025$ and $D/d = 4$. The sample stream attains a small width shortly downstream of the cross-junction. The reduced intensity of the focused stream compared with that of the inlet stream suggests focusing along the depth direction. (b) Snapshot of 3D hydrodynamic focusing of RBCs in a microfluidic device with $D/d = 3$ with $Q_s = 1\ \mu\text{l}/\text{min}$ and $Q_{sh} = 40\ \mu\text{l}/\text{min}$. In the inlet stream, the RBCs are distributed throughout the depth of the channel and hence appear out of the optical focus. After hydrodynamic focusing, the cells flow in a single file and are positioned within the depth-of-field of the microscope objective. (c) Sample images of seven RBCs acquired downstream of the cross-junction using a $40\times$ objective. All the images were captured from below the device using an inverted microscope.

by considering the full width at half maximum (FWHM) of its fluorescence intensity along the channel width. Figure 3(a) shows a comparison of the experimentally measured width w_f of the focused stream with the predictions of numerical simulations, for $D/d = 1$ to 4 and $Q_s/Q_{sh} = 0.014, 0.025, 0.040, 0.050,$ and 0.067 . The width of the focused stream predicted by the simulations are in quantitative agreement with the experimental measurements, suggesting that the sample stream was indeed three-dimensionally focused in our experiments, similar to that in simulations shown in Fig. 2.

C. Imaging of red blood cells

Finally, to demonstrate the applicability of our device for imaging flow cytometry, we hydrodynamically focused a large number of RBCs and imaged them using brightfield microscopy. Based on the experimentally validated numerical simulations, for these set of experiments, we used a microfluidic device with $D/d = 3$ and the sample and sheath-flow rates of $Q_s = 1 \mu\text{l}/\text{min}$ and $Q_{sh} = 40 \mu\text{l}/\text{min}$, respectively. The simulation results presented in Fig. 3 predict that for these conditions, the width and the height of the 3D focused stream would both be $25 \mu\text{m}$, which is about three to four times the disk diameter of an RBC. Our experiments showed that 3D hydrodynamic focusing at these values of D/d and Q_s/Q_{sh} ensured that all the RBCs were always aligned in a single file and were within the depth-of-field of the microscope objective.

Figure 4(b) shows a snapshot of 3D focusing of RBCs visualized using a lower magnification ($10\times$) objective to obtain a larger field-of-view. The cells were imaged near the bottom wall of the channel by locating fiducial marks on the bottom cover plate of the microfluidic device. On the left-hand side of the image, RBCs appear out of focus because they are distributed throughout the depth of the sample inlet channel and most of them are outside the depth-of-field of the objective that is focused near the bottom wall of the channel. As the cells flow from left to right, they get aligned in a single file downstream of the cross-junction and also get positioned within the depth-of-field of the objective. This clearly demonstrates the 3D hydrodynamic focusing capability of our device. Moreover, Fig. 4(b) shows that once the RBCs are the 3D focused downstream of the cross-junction, all of them remain within the optical focus of the objective. Figure 4(c) shows seven representative snapshots of RBCs captured downstream of the cross-junction using a higher magnification ($40\times$) objective at different time instances. All the cells are in-focus due to the positioning of the cells near the bottom wall of the channel. In these experiments, by imaging the cells at various focal planes, we observed that the cells flowed approximately $20 \mu\text{m}$ above the bottom plate. This distance is comparable to the height (d_f) of the focused sample stream, predicted by simulations in Fig. 3.

Finally, to image a large number of RBCs, we chose a small region of interest (ROI) ($350 \mu\text{m}$ length and $36 \mu\text{m}$ width) downstream of the junction, as all the cells flow in a single file, as illustrated schematically in Fig. 5(a). The smaller ROI enabled imaging of cells at a higher frame rate of 102 fps. For this experiment, the cells were imaged using a $20\times$ objective. We captured images of over 300 RBCs in a single experimental run. Figure 5(b) shows the temporal variation of image intensity, integrated over the ROI, as

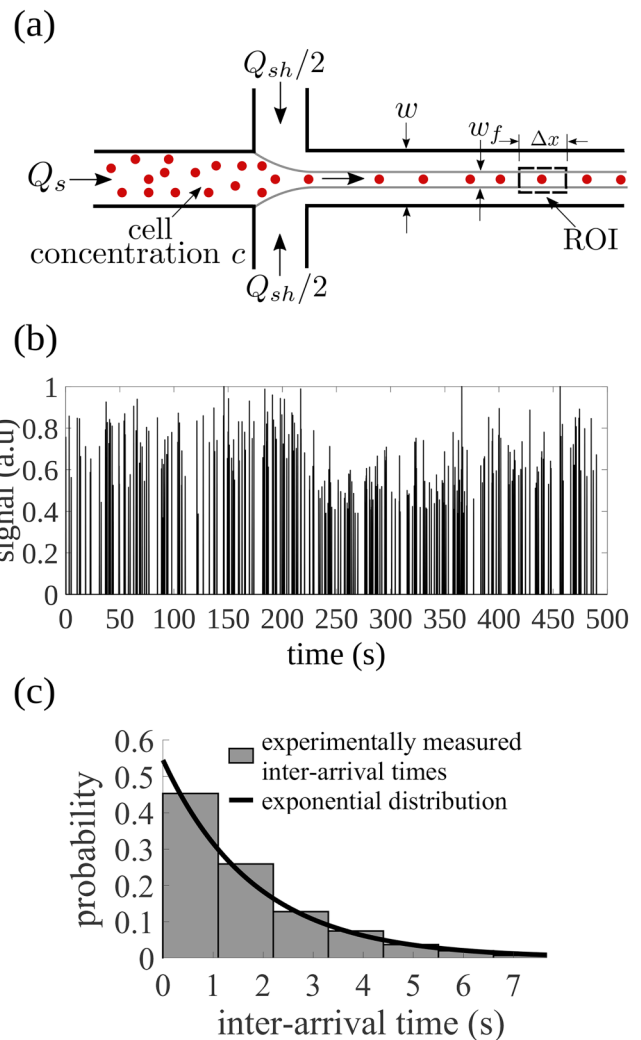


FIG. 5. Arrival times for RBCs to reach the detection volume and the corresponding probability distribution of the inter-arrival time. (a) Schematic illustration of the experiment for imaging a large number of RBCs within a small ROI downstream of the junction. (b) Variation of image intensity integrated over the ROI with time. Each peak corresponds to the presence of an RBC within the detection volume. (c) Histogram showing the distribution of inter-arrival times between the arrival of RBCs within the detection volume. The probability distribution of inter-arrival time follows an exponential distribution with a mean inter-arrival time of 1.83 s.

the cells flow one-by-one through the detection volume. Each peak in the signal intensity corresponds to the presence of an RBC within the detection volume. The data presented in Fig. 5(b) enables counting of cells as performed in conventional flow cytometry, but more importantly, allows determination of the exact time instants when the cells were imaged. As expected, Fig. 5(b) shows that the inter-arrival time between two consecutive cells passing through the detection volume is randomly distributed. To check

whether all the cells passing through the detection volume were imaged at the chosen frame rate of camera, in Fig. 5(c), we plot the probability distribution of the observed inter-arrival times. The histogram of the inter-arrival time shows that the inter-arrival time follows an exponential distribution, which is characteristic of processes wherein events (arrival of cells within the detection volume) occur continuously and independently at a constant average rate. A curve-fit to the data shows that the exponential distribution of the inter-arrival time has a mean inter-arrival time of 1.83 s, which suggests that the chosen frame rate (102 fps) for capturing images was sufficient to image almost all the cells. Because the mean inter-arrival time is over two orders magnitude larger than the time interval between capturing of consecutive images, in the same experiment, even if the sample and sheath-flow rates were increased tenfold, majority of the cells would be imaged correctly. We note that the fact that the cells move independently, as can be inferred from the exponential distribution of inter-arrival times, also suggests that the motion of cells do not affect the fluid flow in the device. That is, the device operation is independent of the location of cells, which is a necessary requirement for robust 3D hydrodynamic focusing of cells.

D. Device throughput, choice of ROI, and camera frame rate

Knowing that the inter-arrival time between the consecutive arrival of cells to the detection volume in our device is exponentially distributed, we can now derive mathematical relations for choosing the size of ROI, and the frame rate of camera so as to avoid events such as arrival of two cells at the same time within the ROI and cells crossing the ROI within the time interval between capturing consecutive images. The exponential distribution of the inter-arrival time, shown in Fig. 5(c), suggests that the arrival of cells within the ROI being imaged occurs at a constant mean rate and independent of the time since the arrival of the last cell to the detection volume. Therefore, the number of cells within the ROI at any given time obeys the Poisson distribution. That is, the probability of the number of cells X within the ROI to be equal to k is given by

$$\Pr(X = k) = \frac{\lambda^k e^{-\lambda}}{k!}, \tag{4}$$

where λ is the mean number of particles within the ROI. For a given concentration of cells c (number of cells per unit volume), the mean number of cells in the axial length Δx of the ROI [shown in Fig. 5(a)] is $\lambda = cw_f d_f \Delta x$. Here, $w_f d_f$ is the cross-sectional area of the 3D focused sample stream, which depends on the sample flow rate Q_s and mean flow velocity of the focused cell stream u_s as $w_f d_f = Q_s / u_s$. The mean number of cells within the ROI can also be written as $\lambda = cQ_s \Delta x / u_s$. To ensure that not more than one cell is present within the ROI at any given time instant, the probability of having either one or no cell within the ROI must be close to 1. Therefore, we can set

$$\Pr(X = 0) + \Pr(X = 1) = (1 + \lambda)e^{-\lambda} > 1 - \epsilon, \tag{5}$$

where $\epsilon \ll 1$. For example, to ensure that the probability of having more than one cell within the ROI is less than 0.5%, $\epsilon = 0.005$. Solving Eq. (5) yields $\lambda \approx \sqrt{2\epsilon}$, which sets a limit on the maximum axial length of the ROI to avoid the arrival of more than one cell at a time. That is,

$$\Delta x \leq \frac{\sqrt{2\epsilon} u_s}{cQ_s}. \tag{6}$$

For low sample flow rates $Q_s \ll Q_{sh}$, the mean flow velocity in the main channel can be approximated as $Q_{sh} / (wd)$. Note that, typically the cells flow close to the bottom wall of the channel, and hence, the mean velocity of the cells u_s can be less than the average flow velocity in the main channel. However, if we assume that the velocity of the cells u_s is same as the mean flow velocity in the main channel $Q_{sh} / (wd)$, the above criterion for choosing Δx can be written as

$$\Delta x \leq \frac{\sqrt{2\epsilon} Q_{sh}}{c w d Q_s}. \tag{7}$$

In addition to this constraint, the axial length of the ROI, Δx , should be larger than the cell dimensions to capture the image of the whole cell.

The frame rate of the camera ($1/\Delta t$) must be chosen such that no cell crosses the ROI within time interval Δt between acquiring two consecutive images. This can be ensured if $\Delta t < \Delta x / u$. Therefore, from Eq. (6), the time interval between capturing two consecutive images Δt must be chosen such that

$$\Delta t < \frac{\Delta x}{u_s} \leq \frac{\sqrt{2\epsilon}}{cQ_s}. \tag{8}$$

In other words, the frame rate of the camera must be greater than $cQ_s / \sqrt{2\epsilon}$ to ensure that all the cells entering the ROI are imaged. Note that cQ_s is the throughput of the device, that is, the number of cells being imaged per unit time and $1/(cQ_s)$ is the mean inter-arrival time. Therefore, for a given choice of Δx and Δt , the throughput of the device is limited by Eqs. (7) and (8). For example, taking $\epsilon = 0.005$, Eq. (8) suggests that the throughput of the device cannot be greater than 1/10th of the frame rate of a camera.

In our experiments of imaging RBCs, presented in Fig. 5, $Q_s = 1 \mu\text{l}/\text{min}$, $Q_{sh} = 40 \mu\text{l}/\text{min}$, $w = 200 \mu\text{m}$, $d = 100 \mu\text{m}$, and $c = 33 \text{ cells}/\mu\text{l}$. Choosing $\epsilon = 0.005$, corresponding to more than 99.5% probability of having one or no cell within the ROI, we obtain $\Delta x \leq 6 \text{ mm}$. The chosen ROI length $\Delta x = 350 \mu\text{m}$ satisfies this criterion and the $\Delta t = 9.8 \text{ ms}$ satisfies the criterion of $\Delta t < \Delta x / u_s \approx 10 \text{ ms}$. The throughput cQ_s of the device in these experiments was 33 cells/min. However, the throughput can be further increased up to 600 cells/min (10 cells/s) corresponding to 1/10-th of the frame rate of camera (102 fps) used in our experiments. The maximum rate of imaging cells using our device can be further increased by employing a camera having a higher frame rate.

V. CONCLUSIONS

We have presented design, characterization, and testing of an inexpensive, sheath-flow based microfluidic device for 3D hydrodynamic focusing of cells in imaging flow cytometry. In contrast to other 3D sheathing devices, our device hydrodynamically focuses the cells in a single file near the bottom wall of the microchannel that allows imaging cells with high magnification and low working distance objectives, without reducing the device dimensions. This allows easy fabrication of our device using techniques such as micromilling, hot embossing, and injection molding. Moreover, the simple device design ensures that tedious alignment of various layers is not required during fabrication. The 3D sheathing strategy employed here is not restricted to a specific range of flow rates. Consequently, our device can be employed for high-throughput cytometers requiring high flow rates as well as for low-cost systems for automated imaging of cells operating at relatively low flow rates.

In this paper, we have characterized the performance of the device with 3D numerical simulations and validated these simulations with experiments of hydrodynamic focusing of a fluorescently dyed sample fluid. The simulations show that the width and the height of the 3D focused sample stream can be controlled independently by varying the heights of the main and the side channels, and the flow rates of the sample and sheath fluids. Based on simulation results, we have also provided useful guidelines for choosing the device dimensions and flow rates for focusing cells of a particular size. Finally, we have demonstrated the applicability of our device for imaging a large number of RBCs using brightfield microscopy. Our microfluidic device is equally applicable for imaging cells of varying sizes using various other imaging techniques such as phase-contrast and fluorescence microscopy, which we will report in future.

ACKNOWLEDGMENTS

We acknowledge the financial support received from the Department of Science and Technology, Ministry of Science and Technology, Government of India (Grant/Award No. ID/MED/34/2016). The authors would like to thank Dr. Krishnamurthy Iyer (University of Minnesota, USA) for helpful discussions and valuable suggestions.

DATA AVAILABILITY

The data that support the findings of this study are available within the article.

REFERENCES

- H. M. Shapiro, *Practical Flow Cytometry* (John Wiley & Sons, 2005).
- M. G. Macey and M. G. Macey, *Flow Cytometry* (Springer, 2007).
- D. Hasegawa, C. Bugarin, M. Giordan, S. Bresolin, D. Longoni, C. Micalizzi, U. Ramenghi, A. Bertaina, G. Basso, F. Locatelli *et al.*, "Validation of flow cytometric phospho-STAT5 as a diagnostic tool for juvenile myelomonocytic leukemia," *Blood Cancer J.* **3**, e160–e160 (2013).
- J. Sandberg, B. Werne, M. Dessing, and J. Lundeberg, "Rapid flow-sorting to simultaneously resolve multiplex massively parallel sequencing products," *Sci. Rep.* **1**, 108 (2011).
- S. C. De Rosa, L. A. Herzenberg, L. A. Herzenberg, and M. Roederer, "11-color, 13-parameter flow cytometry: Identification of human naive T cells by phenotype, function, and T-cell receptor diversity," *Nat. Med.* **7**, 245–248 (2001).
- H.-J. Gross, B. Verwer, D. Houck, and D. Recktenwald, "Detection of rare cells at a frequency of one per million by flow cytometry," *Cytometry* **14**, 519–526 (1993).
- P. Sajeesh and A. K. Sen, "Particle separation and sorting in microfluidic devices: A review," *Microfluid. Nanofluid.* **17**, 1–52 (2014).
- L. A. Herzenberg, D. Parks, B. Sahaf, O. Perez, M. Roederer, and L. A. Herzenberg, "The history and future of the fluorescence activated cell sorter and flow cytometry: A view from stanford," *Clin. Chem.* **48**, 1819–1827 (2002).
- D. A. Ateya, J. S. Erickson, P. B. Howell, L. R. Hilliard, J. P. Golden, and F. S. Ligler, "The good, the bad, and the tiny: A review of microflow cytometry," *Anal. Bioanal. Chem.* **391**, 1485–1498 (2008).
- J. Godin, C.-H. Chen, S. H. Cho, W. Qiao, F. Tsai, and Y.-H. Lo, "Microfluidics and photonics for bio-system-on-a-chip: A review of advancements in technology towards a microfluidic flow cytometry chip," *J. Biophotonics* **1**, 355–376 (2008).
- D. Huh, W. Gu, Y. Kamotani, J. B. Grotberg, and S. Takayama, "Microfluidics for flow cytometric analysis of cells and particles," *Physiol. Meas.* **26**, R73–R98 (2005).
- T. D. Chung and H. C. Kim, "Recent advances in miniaturized microfluidic flow cytometry for clinical use," *Electrophoresis* **28**, 4511–4520 (2007).
- S. Stavrakis, G. Holzner, J. Choo, and A. DeMello, "High-throughput microfluidic imaging flow cytometry," *Curr. Opin. Biotech.* **55**, 36–43 (2019).
- Y. J. Heo, D. Lee, J. Kang, K. Lee, and W. K. Chung, "Real-time image processing for microscopy-based label-free imaging flow cytometry in a microfluidic chip," *Sci. Rep.* **7**, 11651 (2017).
- N. Sundararajan, M. S. Pio, L. P. Lee, and A. A. Berlin, "Three-dimensional hydrodynamic focusing in polydimethylsiloxane (PDMS) microchannels," *J. Microelectromech. Syst.* **13**, 559–567 (2004).
- G. Testa, G. Persichetti, and R. Bernini, "Micro flow cytometer with self-aligned 3D hydrodynamic focusing," *Biomed. Opt. Express* **6**, 54–62 (2015).
- Y.-J. Chiu, S. H. Cho, Z. Mei, V. Lien, T.-F. Wu, and Y.-H. Lo, "Universally applicable three-dimensional hydrodynamic microfluidic flow focusing," *Lab Chip* **13**, 1803–1809 (2013).
- C.-H. Tsai, H.-H. Hou, and L.-M. Fu, "An optimal three-dimensional focusing technique for micro-flow cytometers," *Microfluid. Nanofluid.* **5**, 827–836 (2008).
- S.-C. Lin, P.-W. Yen, C.-C. Peng, and Y.-C. Tung, "Single channel layer, single sheath-flow inlet microfluidic flow cytometer with three-dimensional hydrodynamic focusing," *Lab Chip* **12**, 3135–3141 (2012).
- X. Mao, J. R. Waldeisen, and T. J. Huang, "'Microfluidic drifting'—Implementing three-dimensional hydrodynamic focusing with a single-layer planar microfluidic device," *Lab Chip* **7**, 1260–1262 (2007).
- X. Mao, S.-C. S. Lin, C. Dong, and T. J. Huang, "Single-layer planar on-chip flow cytometer using microfluidic drifting based three-dimensional (3D) hydrodynamic focusing," *Lab Chip* **9**, 1583–1589 (2009).
- A. A. Nawaz, X. Zhang, X. Mao, J. Rufo, S.-C. S. Lin, F. Guo, Y. Zhao, M. Lapsley, P. Li, J. P. McCoy *et al.*, "Sub-micrometer-precision, three-dimensional (3D) hydrodynamic focusing via 'microfluidic drifting'," *Lab Chip* **14**, 415–423 (2014).
- S. Tripathi, A. Kumar, Y. B. V. Kumar, and A. Agrawal, "Three-dimensional hydrodynamic flow focusing of dye, particles and cells in a microfluidic device by employing two bends of opposite curvature," *Microfluid. Nanofluid.* **20**, 34 (2016).
- D. Di Carlo, D. Irimia, R. G. Tompkins, and M. Toner, "Continuous inertial focusing, ordering, and separation of particles in microchannels," *Proc. Natl. Acad. Sci. U.S.A.* **104**, 18892–18897 (2007).
- D. Di Carlo, "Inertial microfluidics," *Lab Chip* **9**, 3038–3046 (2009).